High-resolution matrix-assisted laser desorption ionization–imaging mass spectrometry of lipids in rodent optic nerve tissue

David M. G. Anderson,[1,2] Daniel Mills,[1,2] Jeffrey Spraggins,[1,2] Wendi S. Lambert,[3] David J. Calkins,[3] Kevin L. Schey[1,2]

[1]Department of Biochemistry, Vanderbilt University School of Medicine, Nashville, TN; [2]Mass Spectrometry Research Center, Vanderbilt University School of Medicine, Nashville, TN; [3]Department of Ophthalmology and Visual Sciences, Vanderbilt University School of Medicine, Nashville, TN

Purpose: To develop a method for generating high spatial resolution (10 µm) matrix-assisted laser desorption ionization (MALDI) images of lipids in rodent optic nerve tissue.

Methods: Ice-embedded optic nerve tissue from rats and mice were cryosectioned across the coronal and sagittal axes of the nerve fiber. Sections were thaw mounted on gold-coated MALDI plates and were washed with ammonium acetate to remove biologic salts before being coated in 2,5-dihydroxybenzoic acid by sublimation. MALDI images were generated in positive and negative ion modes at 10 µm spatial resolution. Lipid identification was performed with a high mass resolution Fourier transform ion cyclotron resonance mass spectrometer.

Results: Several lipid species were observed with high signal intensity in MALDI images of optic nerve tissue. Several lipids were localized to specific structures including in the meninges surrounding the optic nerve and in the central neuronal tissue. Specifically, phosphatidylcholine species were observed throughout the nerve tissue in positive ion mode while sulfatide species were observed in high abundance in the meninges surrounding the optic nerve in negative ion mode. Accurate mass measurements and fragmentation using sustained off-resonance irradiation with a high mass resolution Fourier transform ion cyclotron resonance mass spectrometer instrument allowed for identification of lipid species present in the small structure of the optic nerve directly from tissue sections.

Conclusions: An optimized sample preparation method provides excellent sensitivity for lipid species present within optic nerve tissue. This allowed the laser spot size and fluence to be reduced to obtain a high spatial resolution of 10 µm. This new imaging modality can now be applied to determine spatial and molecular changes in optic nerve tissue with disease.

The optic nerve is the conduit for transmitting visual signals along retinal ganglion cell axons to multiple subcortical nuclei involved in various vision-related tasks [1]. These axons are unmyelinated in the retina and remain so in exiting the retina through the optic disc until passing through the optic nerve head [2]. Similar to other nerves within the central nervous system, the optic nerve has associated meninges, including the arachnoidal and pial membranes and the dura, which blends into the sclera. Beyond the nerve head, the fibers become myelinated by oligodendrocytes [3] similar to the white matter in brain and spinal cord tissue [4]. Lipids are a major component of myelin and meninges and support the functional activity of neuronal tissue; therefore, the lipid composition and spatial distribution of lipids in tissues are key to normal nerve function [5]. Optic nerve lipid composition studies indicate that major lipid components include neutral lipid species such as cholesterol, glycosphingolipids such as

cerebrosides, and several glycerophospholipids [5,6]. Changes in optic nerve structure and function are key contributors to glaucoma, the most common optic neuropathy, and include early insult to ganglion cell axons [7]. Many pathogenic features of glaucoma involve spatially specific changes in nerve function and morphology [8,9]. Thus, understanding the spatial pattern of molecular changes is essential for probing molecular mechanisms of disease and identifying new therapeutic targets.

Matrix-assisted laser desorption ionization (MALDI) imaging mass spectrometry (IMS) is a novel imaging modality capable of providing molecular ion maps across tissue surfaces including maps of lipids, proteins, and metabolites [10-12]. In a MALDI-IMS experiment, information about molecular distribution and relative intensity is acquired. In recent years, several papers on imaging mass spectrometry of ocular tissue, including lens, lens capsule, lens lipids, flat mounted retina, and retinal cross sections, have been published [13-19]. Since MALDI-IMS was developed in 1997 by the Caprioli group [20], the technology has progressed rapidly to allow for greater sensitivity and improved spatial resolution. The spatial resolution of MALDI-IMS is currently

Correspondence to: Kevin L. Schey, Department of Biochemistry, Mass Spectrometry Research Center Vanderbilt University, 465 21st Ave So, suite 9160 MRB III, Nashville, TN 37232; Phone: (615) 936-6861; FAX: (615) 343-8372; email: k.schey@vanderbilt.edu

limited by several factors: laser spot size, sensitivity (which is affected by area irradiated and laser power [21]), matrix coverage, and analyte delocalization on the sample surface.

Several recent publications have demonstrated high spatial resolution mass spectrometry imaging of fatty acids, lipids, and proteins with varying sample preparation methods [19,22-25]. Matrix application by sublimation was first shown in 2007 [26] to provide even coverage of matrix over the sample surface without the need for solvents and to produce high-intensity signals for lipid analysis. Washing protocols for tissue sections are an important step in MALDI-IMS sample preparation to remove biologic salts and endogenous compounds within tissue sections; however, washing protocols are not always suitable for lipid analysis due to potential delocalization and removal of lipids. To improve sensitivity toward lipid analysis using MALDI-IMS by reducing the formation of sodium and potassium adducts, ammonium acetate has been shown to improve the mass spectra acquired and the MALDI images generated [27,28].The data presented here demonstrate the MALDI-IMS potential for optic nerve imaging, by imaging mouse and rat optic nerves at high spatial resolution (10 μm) to identify lipid spatial distributions and relative abundance in the tissue.

METHODS

This study was conducted in accordance with regulations set forth in the Association for Research in Vision and Ophthalmology Statement for the Use of Animals in Ophthalmic and Vision Research. Animal protocols were approved by the Institutional Animal Care and Use Committee of the Vanderbilt University Medical Center in accordance with guidelines published in the US Public Health Service Policy on Humane Care and Use of Laboratory Animals.

Whole eyes with the optic nerve attached were removed from Brown Norway rats and C57 mice following cervical dislocation and rapidly frozen in deionized water by placing the eye tissue into a cup fashioned from parafilm that was floated in a weighing boat on top of liquid nitrogen in a
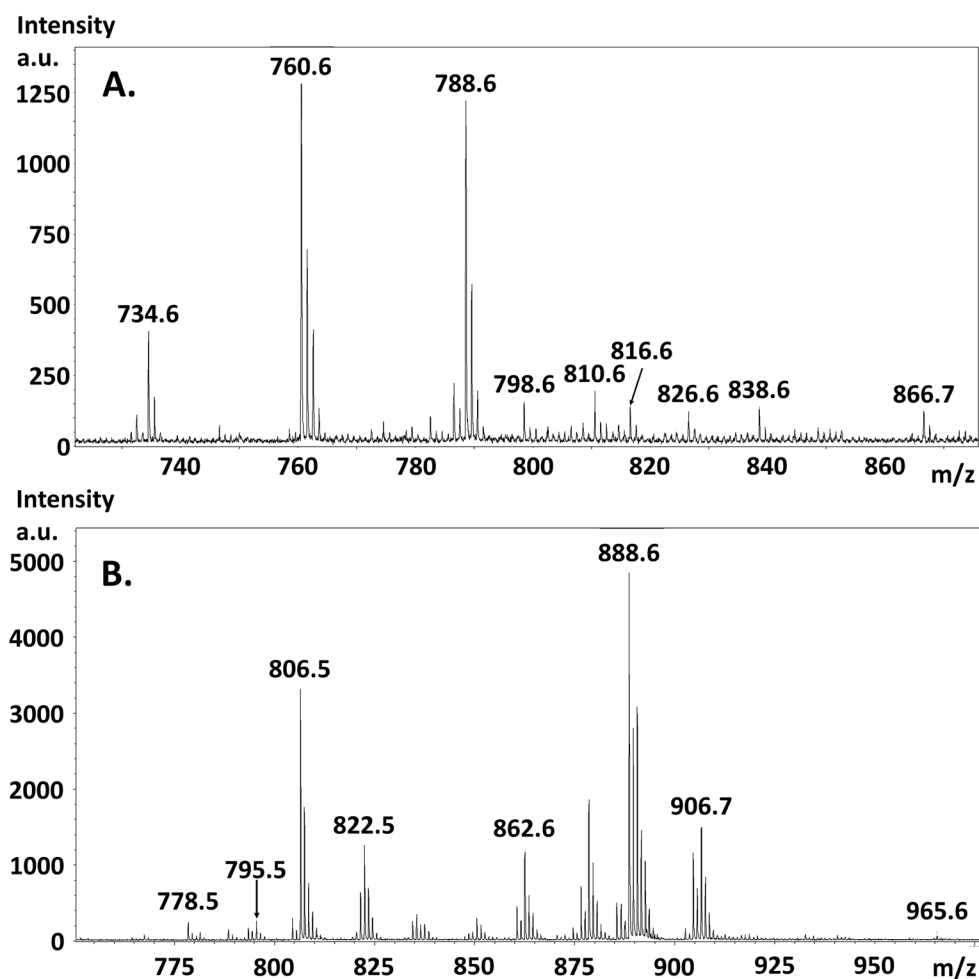

Figure 1. Matrix-assisted laser desorption ionization time-of-flight mass spectra from optic nerve tissue. **A**: Positive ion mode matrix-assisted laser desorption ionization–time-of-flight (MALDI-TOF) mass spectrum from mouse optic nerve tissue showing numerous peaks in the m/z 700–875 region. **B**: Negative ion mode MALDI-TOF mass spectrum from mouse optic nerve tissue showing numerous peaks in the m/z 760–940 region.

TABLE 1. OPTIC NERVE LIPIDS OBSERVED IN POSITIVE ION MODE AND STRUCTURES ASSIGNED BASED ON MASS ACCURACY.

Observed m/z	Theoretical m/z	ppm error	Identification[a]	Molecular Formula
496.3407	496.3398	−1.89	LPC(16:0/0:0)	$C_{24}H_{51}NO_7P+$
524.3708	524.3711	0.58	LPC(18:0/0:0)	$C_{26}H_{55}NO_7P+$
732.5545	732.5538	−0.95	PC(32:1)	$C_{40}H_{79}NO_8P+$
734.5690	734.5694	0.65	PC(32:0)	$C_{40}H_{81}NO_8P++$
758.5691	758.5694	0.43	PC(34:2)	$C_{42}H_{81}NO_8P+$
760.5850	760.5851	0.12	PC(34:1)	$C_{42}H_{83}NO_8P+$
782.5690	782.5694	0.57	PC(36:4)	$C_{44}H_{81}NO_8P+$
786.6007	786.6007	−0.01	PC(36:2)	$C_{44}H_{85}NO_8P+$
788.6161	788.6164	0.42	PC(36:1)	$C_{44}H_{87}NO_8P+$
806.5709	806.5694	−1.85	PC(38:6)	$C_{46}H_{81}NO_8P+$
808.5852	808.5851	−0.19	PC(38:5)	$C_{46}H_{83}NO_8P+$
810.6009	810.6007	−0.15	PC(38:4)	$C_{46}H_{85}NO_8P+$
813.6851	813.6844	−0.90	SM(d18:1/24:1)	$C_{47}H_{94}N_2O_6P+$
832.5863	832.5851	−1.48	PC(40:7)	$C_{48}H_{83}NO_8P+$
834.6000	834.6007	0.83	PC(40:6)	$C_{48}H_{85}NO_8P+$
842.6632	842.6633	0.16	PC(40:2)	$C_{48}H_{93}NO_8P+$
844.6784	844.6790	0.69	PC(40:1)	$C_{48}H_{95}NO_8P+$
853.7277	853.7280	0.29	TG(52:5)	$C_{55}H_{97}O_6+$
855.7419	855.7436	1.99	TG(52:4)	$C_{55}H_{99}O_6+$
870.6948	870.6946	−0.18	PC(42:2)	$C_{50}H_{97}NO_8P+$
879.7439	879.7436	−0.30	TG(54:6)	$C_{57}H_{99}O_6+$
881.7593	881.7593	0.01	TG(54:5)	$C_{57}H_{101}O_6+$
892.6784	892.6790	0.66	PC(44:5)	$C_{52}H_{95}NO_8P+$
907.7738	907.7749	1.23	TG(56:6)	$C_{59}H_{103}O_6+$

[a]Identifications made by mass accuracy alone

polystyrene container. Care was taken to orient the optic nerve so that it could be sectioned along the sagittal axis of the nerve. The ice-embedded sample was then mounted using Tissue-Tek OCT compound (Torrance, CA). Twelve-micron sections were cut with a Leica CM3050S cryostat (Wetzlar, Germany) and thaw mounted onto AB Sciex (Concord, Canada) gold-coated MALDI target plates. The sections were dehydrated in a vacuum desiccator overnight and then washed three times for 30 s each with 100 mM ammonium acetate (Sigma-Aldrich, St. Louis, MO) before being dried again for another 2 h. 2,5-Dihydroxybenzoic acid (DHB; Sigma-Aldrich) was deposited by sublimation onto the samples using a custom sublimation apparatus for 20 min at 54 mTorr pressure at 120 °C. The region containing the optic nerve was imaged in positive and negative ion modes for mouse tissue and positive ion mode for rat tissue using a MALDI-TOF (time-of-flight) mass spectrometer (UltrafleXtreme II, Bruker Daltonics, Billerica, MA) equipped with a Smartbeam II 1 kHz Nd:YAG frequency tripled to 355 nm wavelength.

The laser was set to the minimum spot size with 8% laser power. External calibration was performed with a series of phosphorus clusters before imaging data were acquired [29], and internal calibration, based on masses identified with Fourier transform ion cyclotron resonance (FT-ICR), was performed after the data were acquired to ensure the best mass accuracy from the TOF data. Images were obtained with a spatial resolution of 10×10 μm with 100 laser shots per pixel. Images were generated using Bruker FlexImaging 2.1 software, and the data were normalized to the total ion current.

Lipid identification from the mouse optic nerve tissue was performed using information from two experiments: 1) accurate mass profile scans and 2) tandem mass spectrometry. Both experiments were conducted on tissue sections taken adjacent to those imaged. These data were collected using a MALDI FT-ICR mass spectrometer (9.4 Tesla Apex-Qe, Bruker Daltonics) equipped with an Apollo II dual ion source and the same 355 nm solid-state laser as described above.
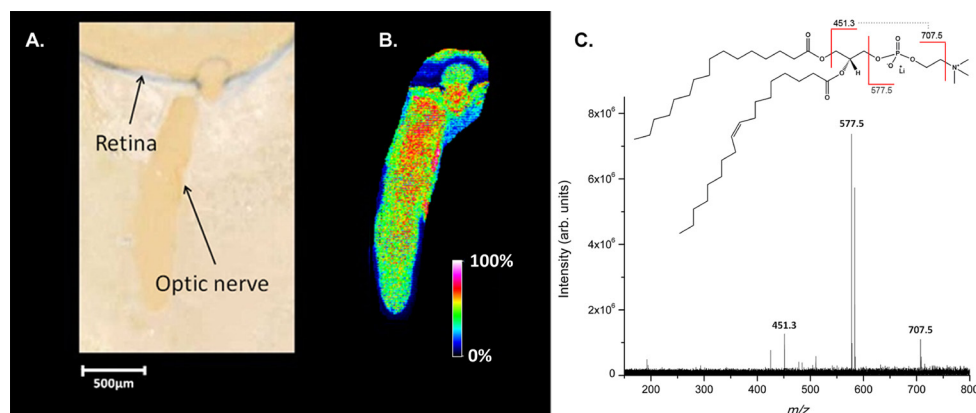
Figure 2. Optical image of tissue and mass spectrometry data of major lipid at m/z 760.6 from mouse optic nerve. **A**: Optical image of ocular tissue section coated with the 2,5-dihydroxybenzoic acid matrix. **B**: Matrix-assisted laser desorption ionization–imaging mass spectrometry (MALDI-IMS) image in positive ion mode at 10 μm spatial resolution of a mouse optic nerve section illustrating the distribution and intensity of a protonated phosphatidylcholine lipid at m/z 760.6. **C**: Product ion spectrum of the lithiated form of m/z 760.6 (m/z 766.6) produced from Fourier transform ion cyclotron resonance mass spectrometer analysis identified as $C_{42}H_{82}NO_8P$ (PC(16:0/18:1)).

External calibration was done using a series of phosphorus clusters (29; P_n, n=5–65) resulting in mass accuracies of better than 2 ppm for all analytes. Tandem mass spectrometry experiments were performed using a combination of continuous accumulation of selected ions (CASI) and sustained off-resonance irradiation collision-induced dissociation (SORI-CID) [30]. CASI (50 laser shots/fill, approximately 100 CASI fills) was used to increase the signal intensities of the mass selected precursor ions in a linear quadrupole (1.5 Da selection window) in the source region of the instrument before fragmentation in the ICR cell. Fragmentation was induced with SORI-CID (pulsed argon, frequency offset: 500 Hz, SORI time: 0.25 s) with a range of SORI power (0.45% to 0.75%) to maximize the number of fragment ions. To promote more structurally informative fragmentation data, 0.2 μl of lithium chloride (100 mM) was pipetted onto the DHB-coated tissue surface of one section for positive ion analysis [31,32], and 0.2 μl of aniline (65 mM) was pipetted onto the sublimed DHB for negative ion analysis. Spectral interpretation was accomplished using LIPID Metabolites

Observed m/z	Theoretical m/z	ppm error	Identification[a]	Molecular Formula
778.5148	778.5145	−0.44	SulfoHex-Cer(d18:1/16:0)	$C_{40}H_{76}NO_{11}$-
788.5449	788.5447	−0.27	PS(36:1)	$C_{42}H_{79}NO_{10}P$-
806.5457	806.5458	0.02	SulfoHex-Cer(d18:1/18:0)	$C_{42}H_{80}NO_{11}$-
810.5299	810.5291	−1.07	PS(38:4)	$C_{44}H_{77}NO_{10}P$-
812.545	812.5447	−0.35	PS(38:3)	$C_{44}H_{79}NO_{10}P$-
816.5745	816.576	1.86	PS(38:1)	$C_{44}H_{83}NO_{10}P$-
834.5292	834.5291	−0.22	PS(40:6)	$C_{46}H_{77}NO_{10}P$-
834.5773	834.5771	−0.24	SulfoHex-Cer(d18:1/20:0)	$C_{44}H_{84}NO_{11}$-
838.5613	838.5604	−1.1	PS(40:4)	$C_{46}H_{81}NO_{10}P$-
857.5187	857.5186	−0.2	PI(36:4)	$C_{45}H_{78}O_{13}P$-
862.6081	862.6084	0.25	SulfoHex-Cer(d18:1/22:0)	$C_{46}H_{88}NO_{11}$-
878.6028	878.6033	0.51	SulfoHex- Cer(d18:1/22:0(2OH))	$C_{46}H_{88}NO_{12}$-
883.5327	883.5342	1.65	PI(38:5)	$C_{47}H_{80}O_{13}P$-
885.5502	885.5499	−0.34	PI(38:4)	$C_{47}H_{82}O_{13}P$-
888.6237	888.624	0.3	SulfoHex-Cer(d18:1/24:1)	$C_{48}H_{92}NO_{11}$-
890.6399	890.6397	−0.29	SulfoHex-Cer(d18:1/24:0)	$C_{48}H_{92}NO_{11}$-
965.516	965.5162	0.18	PI(38:4)	$C_{47}H_{83}O_{16}P$-

TABLE 2. OPTIC NERVE LIPIDS OBSERVED IN NEGATIVE ION MODE AND STRUCTURES ASSIGNED BASED ON MASS ACCURACY.

[a]Identifications made by mass accuracy alone

TABLE 3. SUMMARY OF TANDEM MASS SPECTRA DATA FOR SELECTED ION AT M/Z 766.6[a], PC(16:0/18:1)Li+.

Observed m/z	Identification	Molecular Formula	Theoretical m/z
425.266	[M-59-(18:1)+Li]+	$C_{21}H_{39}LiO_6P+$	425.264
451.282	[M-59-(16:0)+Li]+	$C_{23}H_{41}LiO_6P+$	451.280
478.331	[M-(18:1)+H]+	$C_{24}H_{49}NO6P+$	478.329
484.340	[M-(18:1)+Li]+	$C_{24}H_{48}LiNO_6P+$	484.337
510.357	[M-(16:0)+Li]+	$C_{26}H_{50}LiNO_6P+$	510.353
577.524	[M-183+H]+	$C_{37}H_{69}O_4+$	577.534
583.532	[M-183+Li]+	$C_{37}H_{68}LiO_4+$	583.527
707.527	[M-59+Li]+	$C_{39}H_{73}LiO_8P+$	707.520
766.607 (isolated mass)	[M+Li]+	$C_{42}H_{82}LiNO_8P+$	766.593

[a]+6 Mass unit adjustment is made for the formation of a lithium adduct as a result of adding lithium chloride to the samples before identification.

TABLE 4. SUMMARY OF TANDEM MASS SPECTRA DATA FOR SELECTED ION AT M/Z 806.5, SULFATIDE (D18:1/18:0).

Observed m/z	Identification	Molecular Formula	Theoretical m/z
240.997	[(3′-sulfo)Galβ-H]-	$C_6H_9O_8S-$	241.002
522.271	[M-(18:0)-H]-	$C_{24}H_{44}NO_9S-$	522.274
806.554	[M-H]-	$C_{42}H_{80}NO_{11}S-$	806.546

And Pathways Strategy (LIPID MAPS) to match the accurate mass of the precursor ion and manually by interpreting the fragmentation patterns.

RESULTS

Intense signals were obtained from the meninges surrounding the optic nerve and from the internal nerve tissue using the sublimated DHB matrix. Figure 1A shows a positive ion MALDI mass spectrum from mouse optic nerve tissue with numerous peaks in the m/z 700–875 region. Figure 1B shows a negative ion MALDI mass spectrum from mouse optic nerve tissue with numerous peaks in the m/z 760–940 region. Table 1 lists the lipid signals assigned a structure based on accurate mass measurement and comparison to the LIPID MAPS database. Appendix 1 shows the spatial localization of these lipids within the optic nerve sections. Table 2 lists the lipid signals observed in negative ion mode assigned a structure based on accurate mass measurement and comparison to the LIPDS MAPS database. Appendix 2 shows the spatial localization of these lipids within the optic nerve sections.

Figure 2A displays an optical image of the region of the mouse optic nerve head and optic nerve in positive ion mode after sublimation of the DHB matrix. Figure 2B shows the distribution of a putative protonated lipid at m/z 760.6 acquired in the positive ion mode. The MALDI image indicates that this molecular species is localized in the central

neuronal tissue of the optic nerve with a higher abundance toward the retina. This ion has been identified as a phosphatidylcholine (PC(16:0/18:1) using mass accuracy (0.12 ppm, Table 1) and tandem mass spectrometry as highlighted in Figure 2C. The lithiated form of this ion (m/z 766.6) was selected and accumulated using CASI allowing for high-quality SORI-CID data to be collected. The complete list of observed fragments can be found in Table 3. The observed neutral losses of trimethylamine (m/z 707.5, [M-59+Li]+), ethylene phosphate (m/z 583.5, [M-183+Li]+), and lithium ethylene phosphate (m/z 577.5, [M-183+H]+) are characteristic peaks associated with all glycerophosphocholines [33,34]. Additionally, for lithiated species, the fatty acid in the *sn*-1 position is known to be preferentially lost over the *sn*-2 fatty acyl chain during fragmentation [33,34]. The most abundant fragment ion associated with the loss of a fatty acyl chain was m/z 451.3 ([M-59-(16:0)+Li]+) suggesting that palmitic acid (16:0) is in the *sn*-1 position.

Figure 3A shows the optical image of a mouse optic nerve section after sublimation from which data were acquired in negative ion mode. Figure 3B shows the distribution of a putative deprotonated lipid at m/z 806.5. The MALDI image shows that this molecular species is highly abundant in the meninges surrounding the nerve bundle, with lower abundance in the central neuronal tissue. Figure 3C shows the tandem mass spectrum of m/z 806.5 indicating three major

fragment ions (Table 4). Based on the accurate mass measurements (0.02 ppm, Table 2) and fragmentation patterns, the deprotonated species was identified as sulfatide(d18:1/18:0). The most abundant fragment ion (m/z 241.0) is related to the 3-sulfogalactosyl moiety, and the minor fragment (m/z 522.3) results from the loss of the fatty acyl chain as a ketene followed by loss of water. Both are common fragmentation pathways of sulfatides [35]. Sulfatides account for around 4%–7% of central nervous system myelin by weight and have been shown to be involved in cell signaling pathways and inhibiting axon regeneration [36].

Figure 4A shows an optical image of the region of the mouse optic nerve head and optic nerve imaged after the DHB matrix was applied via sublimation. MALDI imaging data were acquired in positive ion mode, and Figure 4B shows the distribution of the protonated phosphatidylcholine species at m/z 788.6 identified as PC (18:0/18:1; Table 5). The MALDI image shows that this species is localized in the optic nerve head and at the anterior of the optic nerve within the central neuronal tissue. The region of low intensity between the optic nerve head and the optic nerve fiber is an artifact of sectioning, i.e., the nerve fiber was not perfectly aligned within the ice-embedded tissue. The slight kink in the nerve fiber that naturally precedes insertion into the retina resulted in no nerve tissue being present in the region indicated by the white arrow. Figure 4C shows the distribution of the protonated phosphatidylcholine species (PC(16:0/16:0) Table
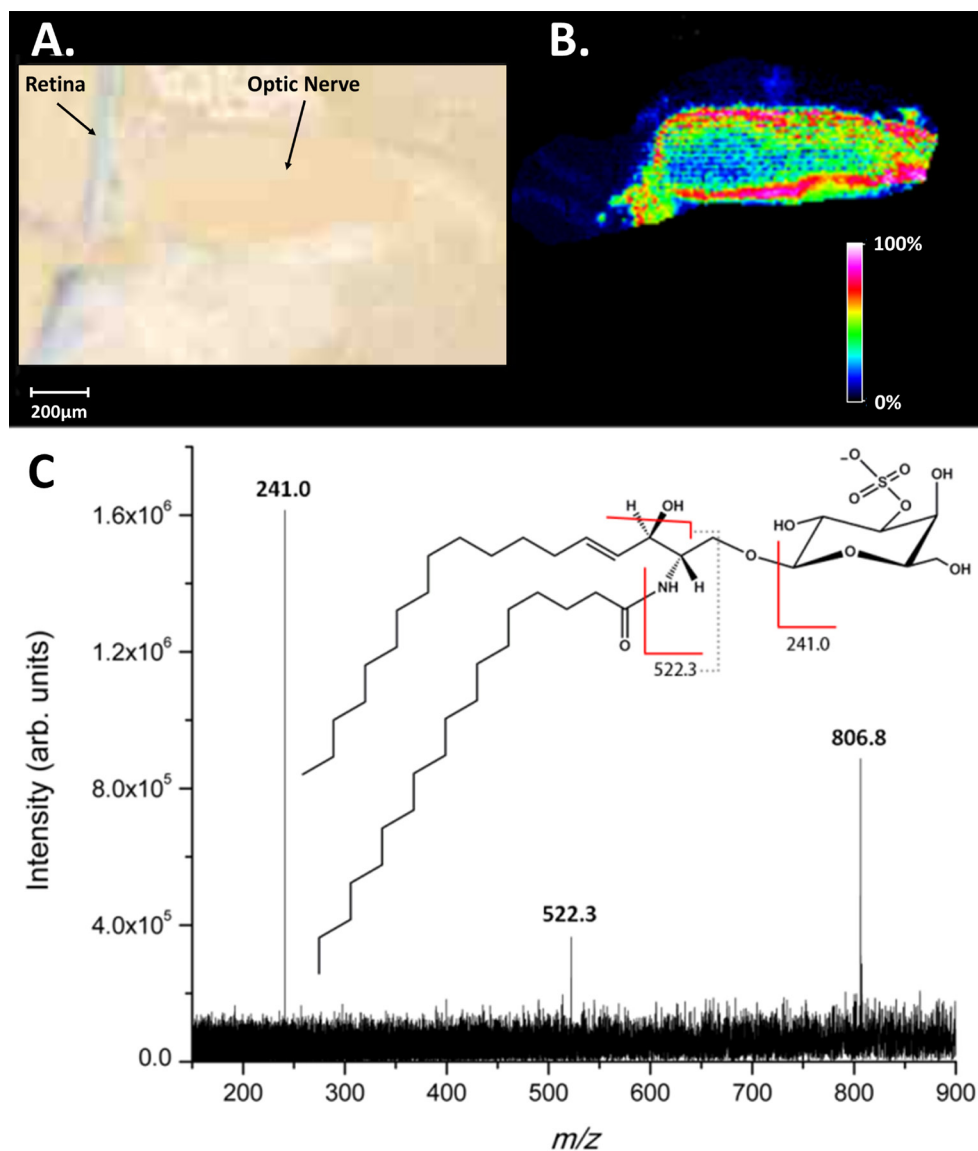

Figure 3. Optical image of tissue and mass spectrometry data of major lipid at m/z 806.5 from mouse optic nerve. **A**: Optical image of ocular tissue section coated with the 2,5-dihydroxybenzoic acid matrix. **B**: Matrix-assisted laser desorption ionization–imaging mass spectrometry (MALDI-IMS) image showing the distribution of the deprotonated sphingolipid species at m/z 806.5. **C**: product ion spectrum of m/z 806.5 identified as $C_{42}H_{80}NO_{11}S$ (Sulfatide (d18:1/18:0)).
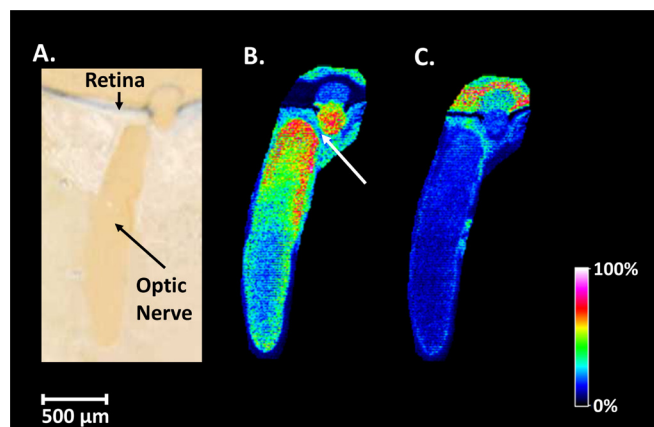
Figure 4. Optical and mass spectrometry images of mouse optic nerve tissue. **A**: Optical image of mouse ocular tissue section coated with the 2,5-dihydroxybenzoic acid matrix. **B**: Matrix-assisted laser desorption ionization–imaging mass spectrometry (MALDI-IMS) image in positive ion mode at 10 µm spatial resolution of a mouse optic nerve illustrating the distribution and intensity of a protonated phosphatidylcholine species $C_{44}H_{86}NO_8P$ (PC(18:1/18:0)) at m/z 788.6. **C**: MALDI-IMS image illustrating the distribution and intensity of a protonated phosphatidylcholine species $C_{40}H_{80}NO_8P$ (PC (16:0:16:0)) at m/z 734.6.

6) at m/z 734.6; the MALDI image shows that this species is located in the optic nerve head.

Figure 5A shows an optical image of the region of the mouse optic nerve head and optic nerve imaged after the matrix was applied via sublimation. MALDI imaging data were acquired in negative ion mode, and Figure 5B shows the distribution of a deprotonated sphingolipid species at m/z 890.6 with the molecular formula $C_{48}H_{92}NO_{11}S$, sulfatide (d18:1/24:0; Table 7). This sulfatide has a high abundance throughout the majority of the neuronal tissue, with the highest abundance in the meninges surrounding the optic nerve. Figure 5C shows the distribution of another deprotonated sphingolipid species at m/z 878.6 with the molecular formula $C_{46}H_{88}NO_{12}S$, sulfatide (d18:0/22:0(2OH); Table 8). The MALDI image shows that this species is present with lower abundance than sulfatide (d18:1/24:0) and is predominantly observed in the meninges surrounding the nerve fiber away from the retina and optic nerve head.

To image coronal sections, a slightly larger rat optic nerve was examined. Figure 6A shows the distribution of a protonated lipid at m/z 810.6 (PC(18:0/20:4; Table 9) in a cross section from a rat optic nerve fiber with high abundance present in the optic nerve sheath, in the wall of a vein

TABLE 5. SUMMARY OF TANDEM MASS SPECTRAL DATA FOR SELECTED ION AT M/Z 794.6ᴬ, PC(18:0/18:1)Lɪ⁺.

Observed m/z	Identification[a]	Molecular Formula	Theoretical m/z
451.283	[M-59-(18:0)+H]+	$C_{23}H_{41}LiO_6P+$	451.280
506.364	[M-(18:1)+H]+	$C_{26}H_{53}NO_6P+$	506.361
510.355	[M-(18:0)+Li]+	$C_{26}H_{50}LiNO_6P+$	510.353
605.555	[M-183+H]+	$C_{39}H_{73}O_4+$	605.550
611.564	[M-183+Li]+	$C_{39}H_{72}LiO_4+$	611.559
735.560	[M-59+Li]+	$C_{41}H_{77}LiO_8P+$	735.551
794.638	[M+Li]+	$C_{44}H_{86}LiNO_8P+$	794.625

[a]+6 Mass unit adjustment is made for the formation of a lithium adduct as a result of adding lithium chloride to the samples before identification.

TABLE 6. SUMMARY OF TANDEM MASS SPECTRAL DATA FOR SELECTED ION AT M/Z 740.6ᴬ, PC(16:0/16:0)Lɪ⁺.

Observed m/z	Identification[a]	Molecular Formula	Theoretical m/z
425.266	[M-59-(16:0)+Li]+	$C_{21}H_{39}LiO_6P+$	425.264
551.507	[M-183+H]+	$C_{35}H_{67}O_4+$	551.503
557.518	[M-183+Li]+	$C_{35}H_{66}LiO_4+$	557.512
740.59	[M+Li]+	$C_{40}HLiNO_8P+$	740.578

[a]+6 Mass unit adjustment is made for the formation of a lithium adduct as a result of adding lithium chloride to the samples before identification.
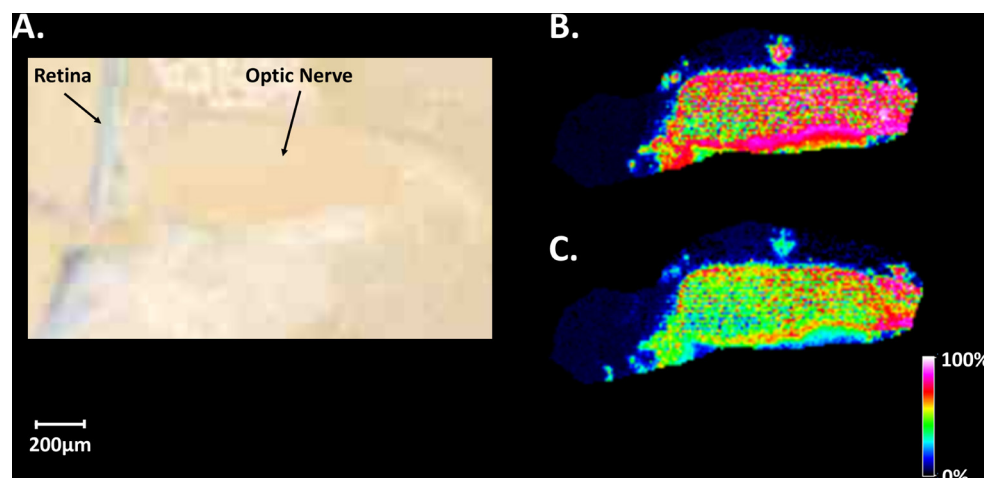
Figure 5. Optical and mass spectrometry images of mouse optic nerve tissue. **A**: Optical image of mouse ocular tissue section coated with the 2,5-dihydroxybenzoic acid matrix. **B**: Matrix-assisted laser desorption ionization–imaging mass spectrometry (MALDI-IMS) image in negative ion mode at 10 µm spatial resolution of a mouse optic nerve illustrating the distribution and intensity of a deprotonated sphingolipid species $C_{48}H_{92}NO_{11}S$ sulfatide (d18:1:24:0)) at m/z 890.6. **C**: MALDI-IMS image illustrating the distribution and intensity of a deprotonated sphingolipid species $C_{46}H_{88}NO_{12}S$ (Sulfatide(d18:0/22:0(2OH)) at m/z 878.6.
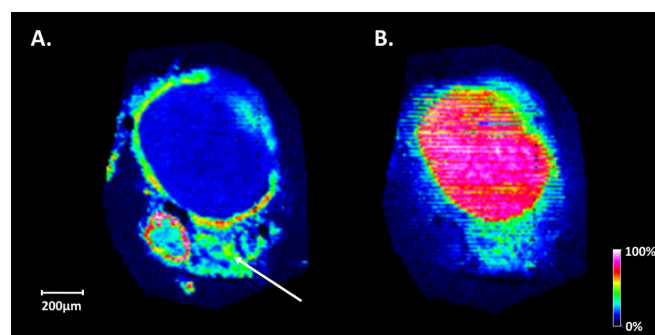

Figure 6. Mass spectrometry images of rat optic nerve tissue. **A**: Matrix-assisted laser desorption ionization–imaging mass spectrometry (MALDI-IMS) image showing the distribution of PC(18:0/20:4) at m/z 810.6 located in the meninges, connective tissue, and the wall of a blood vessel running parallel to the optic nerve fiber. **B**: MALDI-IMS image of PC(18:0/18:1) at m/z 788.6 located in the optic nerve.

TABLE 7. SUMMARY OF TANDEM MASS SPECTRAL DATA FOR SELECTED ION AT M/Z **890.7**, SULFATIDE(D18:1/24:0).

Observed m/z	Identification[a]	Molecular Formula	Theoretical m/z
240.997	[(3′-sulfo)Galβ-(H2O)-H]-	$C_6H_9O_8S-$	241.002
522.279	[M-(24:0)-H]-	$C_{24}H_{44}NO_9S-$	522.274
890.649	[M-H]-	C48H92NO11S-	890.640

TABLE 8. SUMMARY OF TANDEM MASS SPECTRAL DATA FOR SELECTED ION AT M/Z **878.6**, SULFATIDE(D18:0/22:0(2OH)).

Observed m/z	Identification[a]	Molecular Formula	Theoretical m/z
240.997	[(3′-sulfo)Galβ-(H2O)-H]-	$C_6H_9O_8S-$	241.002
259.007	[(3′-sulfo)Galβ-H]-	$C_6H_{11}O_9S-$	259.013
507.266	[M-(22:0(OH))-(OH)-(NH3)-H]-	$C_{24}H_{43}O_9S-$	507.263
522.277	[M-(22:0(OH))-(OH)-H]-	$C_{24}H_{44}NO_9S-$	522.274
540.289	[M-(22:0(OH))-H]-	$C_{24}H_{46}NO_{10}S-$	540.285
568.284	[M-(C21H42O)-H]-	$C_{25}H_{46}NO_{11}S-$	568.28
878.618	[M-H]-	$C_{46}H_{88}NO_{12}S-$	878.603

TABLE 9. SUMMARY OF TANDEM MASS SPECTRAL DATA FOR SELECTED ION AT M/Z 816.6ᵃ, PC(18:0/20:4)Lɪ⁺.

Observed m/z	Identificationᵃ	Molecular Formula	Theoretical m/z
532.338	[M-(18:0)+Li]+	$C_{21}H_{39}LiO_6P+$	532.337
633.546	[M-183+Li]+	$C_{41}H_{70}LiO_4+$	633.543
757.539	[M-59+Li]+	$C_{43}H_{75}LiO_8+$	757.535
816.612	[M+Li]+	$C_{44}H_{86}LiNO_8P+$	816.609

ᵃ+6 Mass unit adjustment is made for the formation of a lithium adduct as a result of adding lithium chloride to the samples before identification.

TABLE 10. SUMMARY OF TANDEM MASS SPECTRAL DATA FOR SELECTED ION AT M/Z 794.636ᵃ, PC(18:0/18:1)Lɪ⁺.

Observed m/z	Identificationᵃ	Molecular Formula	Theoretical m/z
451.282	[M-59-(18:0)+H]+	$C_{23}H_{41}LiO_6P+$	451.28
506.361	[M-(18:1)+H]+	$C_{26}H_{53}NO_6P+$	506.361
510.354	[M-(18:0)+Li]+	$C_{26}H_{50}LiNO_6P+$	510.353
605.554	[M-183+H]+	$C_{39}H_{73}O_4+$	605.55
611.563	[M-183+Li]+	$C_{39}H_{72}LiO_4+$	611.559
735.559	[M-59+Li]+	$C_{41}H_{77}LiO_8P+$	735.551
794.636	[M+Li]+	$C_{44}H_{86}LiNO_8P+$	794.625

ᵃ+6 Mass unit adjustment is made for the formation of a lithium adduct as a result of adding lithium chloride to the samples before identification.
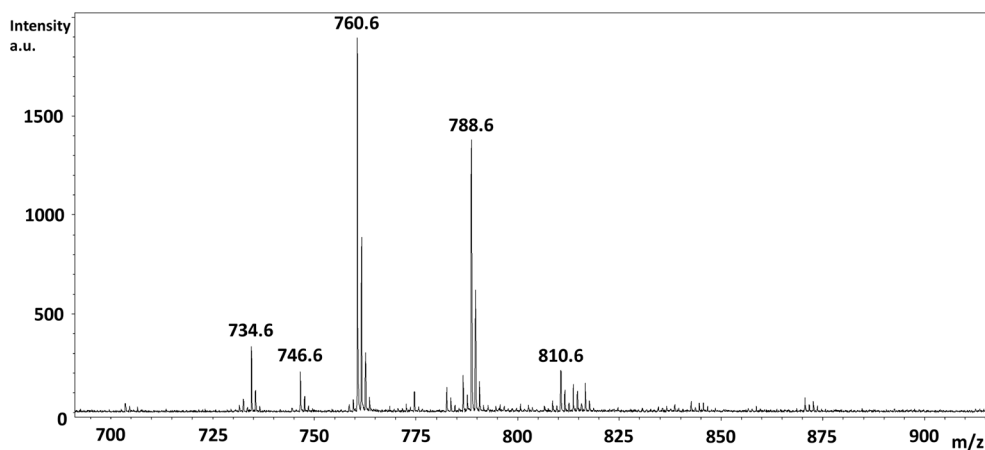

Figure 7. Matrix-assisted laser desorption ionization mass spectrum from rat optic nerve tissue. Positive ion mode matrix-assisted laser desorption ionization–time-of-flight (MALDI-TOF) mass spectrum from rat optic nerve tissue showing numerous peaks in the m/z 700–875 region.

alongside the optic nerve fiber and a lower abundance present in the meninges surrounding the optic nerve and the connective tissue between the two (indicated by the arrow). Figure 6B shows the distribution of a protonated lipid at m/z 788.6 (PC(18:0/18:1; Table 10) in the central region of the optic nerve with high abundance throughout the tissue. Figure 7 shows a positive ion MALDI mass spectrum from this tissue.

DISCUSSION

Using high spatial resolution (10×10 μm) MALDI imaging mass spectrometry, we demonstrated localized and identified lipid species and their relative abundances within small

structures of mouse and rat optic nerve tissue of 200–600 μm diameter. The sample preparation method described allowed images to be acquired at 10 μm spatial resolution. Images acquired in positive ion mode provided the distribution of several phosphatidylcholine species and one sphingomyelin associated with the internal axon fibers and surrounding meninges of the optic nerve (Table 1 and Appendix 1). The data observed in negative ion mode indicated several sulfatides along with other lipid species including phosphoinositols and a phosphoinositol monophosphate (Table 2 and Appendix 2) with the highest abundance within the meninges surrounding the nerve, the internal axon fibers, and the optic

nerve head region. Murphy et al. [37] demonstrated that these lipid species are expected when using DHB as a matrix. An alternative matrix such as 1,5-diaminonaphthalene has been shown to provide excellent sensitivity at high spatial resolutions and more variety toward lipid species [25] that could be amenable to this tissue type and disease model tissue. As optic nerve tissue is regarded as an extension of the white matter of the brain, these lipid species have been previously described in several MALDI-IMS, time-of-flight secondary ion mass spectrometry (TOF-SIMS), and electrospray ionization mass spectrometry (ESI-MS) publications from spinal cord tissue and rodent brain [36,38-40]. The data presented demonstrate the potential use of MALDI-IMS to compare lipid composition, abundance, and localization in optic nerve tissue in various disease models.

Although not much is known about the functionality of lipids in the central nervous system, the localization of protein and lipid changes within the optic nerve and retina in models of glaucoma is relevant to pathology. Degeneration of retinal ganglion cell bodies and their axons is not uniform, but rather occurs in a sectorial pattern from one retinotopic region to the next. Wedge- or fan-shaped regions of degeneration have been observed in the DBA/2J mouse model of glaucoma, as well as in different acute models [9,41-44]. These sectorial losses in the retina also correspond to regional loss of retinal ganglion cell axons within the optic nerve [8,45] and to focal deficits in axonal transport within the superior colliculus [7,46]. Interestingly, the sectorial pattern of retinal ganglion cell degeneration has also been observed in human glaucomatous retinas [47].

The method of sublimation to apply the matrix provides a small crystal in a dense lattice. This property combined with removing the biologic salts from the tissue sections with the wash step, provided sufficient sensitivity allowing for a small (<10 µm) laser spot to be used. This method allows for reliable imaging analysis and identification of endogenous lipids within small tissue structures. Selective ion accumulation in the hexapole region of the FT-ICR using the CASI method before fragmentation made lipid identification easier as the signal intensity for the fragments were significantly improved. In conclusion, the MALDI-IMS technology shows great promise for generating spatial and molecular information in diseases affecting optic nerve structure and function, leading to information that can be used to understand molecular mechanisms of disease and to develop new therapeutic strategies.

APPENDIX 1.

Matrix-assisted laser desorption ionization–imaging mass spectrometry images of selected lipids observed from mouse optic nerve tissue in positive ion mode. Lipid assignments were made based on mass accuracy alone. To access the data, click or select the words "Appendix 1."

APPENDIX 2.

Matrix-assisted laser desorption ionization–imaging mass spectrometry images of selected lipids from mouse optic nerve tissue observed in negative ion mode. Lipid assignments were based on mass accuracy alone. To access the data, click or select the words "Appendix 2."

REFERENCES

1. Mullins RF, Skeie JM. Essentials of Retinal Morphology Animals Models for Retinal Diseases. Vol. 46. Neuromethods New York City (NY) 2010.

2. Brooks DE, Komáromy AM, Källberg ME. Comparative retinal ganglion cell and optic nerve morphology. Vet Ophthalmol 1999; 2:3-11. [PMID: 11397238].

3. Butt AM, Pugh M, Hubbard P, James G. Functions of optic nerve glia: axoglial signaling in physiology and pathology. Eye (Lond) 2004; 18:1110-21. [PMID: 15534596].

4. Liu GT, Volpe NJ, Galetta SL. Neuro-Ophthalmology. 2nd edition. Philadelphia (PA): Saunders/Elsevier 2010.

5. Das SK, Steen ME, McCullough MS, Bhattacharyya DK. Composition of Lipids of Bovine Optic Nerve. Lipids 1978; 13:679-84. [PMID: 723480].

6. Greiner CAM, Greiner JV, Leahy CD, Auerbach DB, Marcus MD, Davies LH, Rodriguez W, Glonek T. Distribution of membrane phospholipids in the rabbit neural retina, optic nerve head and optic nerve. Int J Biochem Cell Biol 1995; 27:21-8. [PMID: 7757879].

7. Sappington RM, Carlson BJ, Crish SD, Calkins DJ. The microbead occlusion model: A paradigm for induced ocular hypertension in rats and mice. Invest Ophthalmol Vis Sci 2010; 51:207-16. [PMID: 19850836].

8. Howell GR, Libby RT, Jakobs TC, Smith RS, Phalan FC, Barter JW, Barbay JM, Marchant JK, Mahesh N, Porciatti V, Whitmore AV, Masland RH, John SWM. Axons of retinal ganglion cells are insulted in the optic nerve early in DBA/2J glaucoma J Cell Biol 2007; 179:1523-37. [PMID: 18158332].

9.   Soto I, Oglesby E, Buckingham BP, Son JL, Roberson EDO, Steele MR, Inman DM, Vetter ML, Horner PJ, Marsh-Armstrong N. Retinal ganglion cells downregulate gene expression and lose their axons with the optic nerve head in a mouse glaucoma model. J Neurosci 2008; 28:548-61. [PMID: 18184797].

10. Puolitaival SM, Burnum EK, Cornett SC, Caprioli RM. Solvent-free matrix dry-coating for MALDI imaging of phospholipids. J Am Soc Mass Spectrom 2008; 19:882-6. [PMID: 18378160].

11. Seeley EH, Caprioli RM. Molecular imaging of proteins in tissues by mass spectrometry. Proc Natl Acad Sci USA 2008; 105:18126-31. [PMID: 18776051].

12. Stoeckli M, Staab D, Schweitzer A. Compound and metabolite distribution measured by MALDI mass spectrometry imaging in whole body tissue sections. Int J Mass Spectrom 2007; 2:195-202. .

13. Grey AC, Chaurand P, Caprioli RM, Schey KL. MALDI imaging mass spectrometry of integral membrane proteins from ocular lens and retinal tissue. J Proteome Res 2009; 8:3278-83. [PMID: 19326924].

14. Ronci M, Sharma S, Chataway T, Burdon KP, Martin S, Craig JE, Voelcker NH. MALDI-MS-imaging of whole human lens capsule. J Proteome Res 2011; 10:3522-9. [PMID: 21663315].

15. Vidová V, Pól J, Volný M, Novák P, Havlíček V, Wiedmer SK, Holopainen JM. Visualizing spatial lipid distribution in porcine lens by MALDI imaging high-resolution mass spectrometry. J Lipid Res 2010; 51:2295-302. [PMID: 20388918].

16. Deeley JM, Hankin JA, Friedrich MG, Murphy RC, Truscott RJW, Mitchell TW, Blanksby SJ. Sphingolipid distribution changes with age in the human lens J Lipid Res 2010; 51:2753-60. [PMID: 20547889].

17. Grey AC, Crouch RK, Koutalos Y, Schey KL, Ablonczy Z. Spatial localization of A2E in the retinal pigment epithelium. Invest Ophthalmol Vis Sci 2011; 52:3926-33. [PMID: 21357388].

18. Garrett TJ, Menger RF, Dawson WW, Yost RA. Lipid analysis of flat-mounted eye tissue by imaging mass spectrometry with identification of contaminants in preservation. Anal Bioanal Chem 2011; 401:103-13. [PMID: 21556752].

19. Roy MC, Nakanishi H, Takahashi K, Nakanishi S, Kajihara S, Hayasaka T, Setou M, Ogawa K, Taguchi R, Naito T. Salamander retina phospholipids and their localization by MALDI imaging mass spectrometry at cellular size resolution. J Lipid Res 2011; 52:463-70. [PMID: 21149645].

20. Caprioli RM, Farmer TB, Gile J. Molecular imaging of biological samples: location of peptides and proteins using MALDI-TOF MS. Anal Chem 1997; 69:4751-60. [PMID: 9406525].

21. Guenther S, Koestler M, Schulz O, Spengler B. Laser spot size and laser power dependence of ion formation in higher resolution MALDI imaging. Int J Mass Spectrom 2010; 294:7-15. .

22. Deutskens F, Junhai Y, Caprioli RM. High spatial resolution imaging mass spectrometry and classical histology on a single tissue section. J Mass Spectrom 2011; 46:568-71. [PMID: 21630385].

23. Yang J, Caprioli RM. Matrix sublimation/recrystallization for imaging proteins by mass spectrometry at high spatial resolution. Anal Chem 2011; 83:5728-34. [PMID: 21639088].

24. Guenther S, Römpp A, Kummer W, Spengler B. AP-MALDI Imaging of neuropeptides in mouse pituitary gland with 5 μm spatial resolution and high mass accuracy. Int J Mass Spectrom 2011; 305:228-37. .

25. Thomas A, Charbonneau JL, Fournaise E, Chaurand P. Sublimation of new matrix candidates for high spatial resolution imaging mass spectrometry of lipids: enhanced information in both positive and negative polarities after 1,5-diaminonapthalene deposition. Anal Chem 2012; 84:2048-54. [PMID: 22243482].

26. Hankin JA, Barkley RM, Murphy RCJ. Sublimation as a method of matrix application for mass spectrometric imaging J Am Soc Mass Spectrom 2007; 18:1646-52. [PMID: 17659880].

27. Wang HY, Liu CB, Wu WU. A Simple Desalting Method for Direct MALDI Mass Spectrometry Profiling of Tissue Lipids. J Lipid Res 2011; 52:840-9. [PMID: 21266365].

28. Angel PM, Spraggins JM, Baldwin HS, Caprioli RM. Enhanced Sensitivity for High Spatial Resolution Lipid Imaging by Negative Ion Mode MALDI Imaging Mass Spectrometry. Anal Chem 2012; 84:1557-64. [PMID: 22243218].

29. Sla´dkova´ K, Housˇka J, Havel J. Laser desorption ionization of red phosphorus clusters and their use for mass calibration in time-of-flight mass spectrometry. Rapid Commun Mass Spectrom 2009; 23:3114-8. [PMID: 19714708].

30. Herrmann KA, Somogyi A, Wysocki VH, Drahos L, Vékey K. Combination of sustained off-resonance irradiation and on-resonance excitation in FT-ICR. Anal Chem 2005; 77:7626-38. [PMID: 16316170].

31. Burnum KE, Cornett DS, Puolitaival SM, Milne SB, Myers DS, Tranguch S, Brown HA, Dey SK, Caprioli RM. Spatial and temporal alterations of phospholipids determined by mass spectrometry during mouse embryo implantation. J Lipid Res 2009; 50:2290-8. [PMID: 19429885].

32. Cerruti CD, Touboul D, Guérineau V, Petit VW, Laprévote O, Brunelle A. MALDI imaging mass spectrometry of lipids by adding lithium salts to the matrix solution. Anal Bioanal Chem 2011; 401:75-87. [PMID: 21380605].

33. Hsu F-F, Turk J. Electrospray ionization/tandem quadrupole mass spectrometric studies on phosphatidylcholines: The fragmentation processes. J Am Soc Mass Spectrom 2003; 14:352-63. [PMID: 12686482].

34. Hsu F-F, Turk J. Electrospray ionization with low-energy collisionally activated dissociation tandem mass spectrometry of glycerophospholipids: mechanisms of fragmentation and structural characterization. J Chromatogr B Analyt Technol Biomed Life Sci 2009; 877:2673-95. [PMID: 19269264].

35. Hsu F-F, Turk J. Studies on sulfatides by quadrupole ion-trap mass spectrometry with electrospray ionization: structural characterization and the fragmentation processes that include an unusual internal galactose residue loss and the classical charge-remote fragmentation. J Am Soc Mass Spectrom 2004; 15:536-46. [PMID: 15047058].

36. Murphy RC, Hankin JA, Barkley RM. Imaging of Lipid Species by MALDI Mass Spectrometry. J Lipid Res 2009; 50:S317-22. [PMID: 19050313].

37. Hanada M, Sugiura Y, Shino R, Masaki N, Imagama S, Ishiguro N, Matsuyama Y, Setou M. Spatiotemporal alteration of phospholipids and prostaglandins in a rat model of spinal cord injury. Anal Bioanal Chem 2012; 403:1873-84. [PMID: 22415026].

38. Sjövall P, Lausmaa J, Johansson B. Mass spectrometric imaging of lipids in brain tissue. Anal Chem 2004; 76:4271-8. [PMID: 15283560].

39. Hankin JA, Murphy RC. The relationship between MALDI IMS intensity and measured quantity of selected phospholipids in rat brain sections. Anal Chem 2010; 82:8476-84. [PMID: 20853893].

40. Winzeler AM, Mandemakers WJ, Sun MJ, Stafford M, Phillips CT, Barres BA. The lipid sulfatide is a novel myelin-associated inhibitor of CNS axon outgrowth. J Neurosci 2011; 31:6481-92. [PMID: 21525289].

41. Jakobs TC, Libby RT, Ben Y, John SW, Masland RH. Retinal ganglion cell degeneration is topological but not cell type specific in DBA/2J mice. J Cell Biol 2005; 171:313-25. [PMID: 16247030].

42. Filippopoulos T, Danias J, Chen B, Podos SM, Mittag TW. Topographic and morphologic analyses of retinal ganglion cell loss in old DBA/2NNia mice. Invest Ophthalmol Vis Sci 2006; 47:1968-74. [PMID: 16639004].

43. Wax MB, Tezel G, Yang J, Peng G, Patil RV, Agarwal N, Sappington RM, Calkins DJ. Induced autoimmunity to heat shock proteins elicits glaucomatous loss of retinal ganglion cell neurons via activated T cell-derived Fas-ligand. J Neurosci 2008; 28:12085-96. [PMID: 19005073].

44. Soto I, Pease ME, Son JL, Shi X, Quigley HA, Marsh-Armstrong N. Retinal Ganglion Cell Loss in a Rat Ocular Hypertension Model Is Sectorial and Involves Early Optic Nerve Axon Loss. Invest Ophthalmol Vis Sci 2011; 52:434-41. [PMID: 20811062].

45. Schlamp CL, Li Y, Dietz JA, Janssen KT, Nickells RW. Progressive ganglion cell loss and optic nerve degeneration in DBA/2J mice is variable and asymmetric. BMC Neurosci 2006; 7:1-14. [PMID: 16393337].

46. Lambert WS, Ruiz L, Crish SD, Wheeler LA, Calkins DJ. Brimonidine prevents axonal and somatic degeneration of retinal ganglion cell neurons. Mol Neurodegener 2011; 6:1-13. [PMID: 21211002].

47. Lei Y, Garrahan N, Hermann B, Fautsch MP, Johnson DH, Hernandez MR, Boulton M, Morgan JE. Topography of neuron loss in the retinal ganglion cell layer in human glaucoma. Br J Ophthalmol 2009; 93:1676-9. [PMID: 19671529].